A SECOND-ORDER VARIATIONAL FRAMEWORK FOR JOINT DEPTH MAP ESTIMATION AND IMAGE DEHAZING

Ryan Wen Liu[1,2] *Shengwu Xiong*[3,⋆] *Huisi Wu*[4]

[1]School of Navigation, Wuhan University of Technology, Wuhan 430063, China
[2]Key Laboratory of Intelligent Perception and Systems for High-Dimensional Information of Ministry of Education, Nanjing University of Science and Technology, Nanjing 210094, China
[3]School of Computer Science and Technology, Wuhan University of Technology, Wuhan 430070, China
[4]College of Computer Science and Software Engineering, Shenzhen University, Shenzhen 518060, China
⋆Corresponding Author: xiongsw@whut.edu.cn

ABSTRACT

Outdoor images captured in poor weather conditions (e.g., fog or haze) commonly suffer from reduced contrast and visibility. Increasing attention has recently been paid to single image dehazing, i.e., improving image contrast and visibility. It is generally thought that the dehazing performance highly depends on the accurate depth information. In this work, we first obtain the initial depth map by using the popular dark channel prior. A unified second-order variational framework is then proposed to refine the depth map and restore the haze-free image. The introduced second-order framework has the capacity of preserving important structures in both depth map and haze-free image. Furthermore, the proposed framework performs well for several different types of haze situations. The resulting optimization problems related to depth map estimation and latent image restoration can be effectively handled using the primal-dual algorithm under a two-step numerical framework. The effectiveness of our proposed method has been demonstrated by comparing the imaging performance with several state-of-the-art dehazing methods.

Index Terms— Image dehazing, depth map, variational method, total generalized variation, primal-dual algorithm

1. INTRODUCTION

Outdoor images captured in foggy or hazy weather conditions commonly suffer from reduced contrast and visibility since the light is easily attenuated and scattered by suspended particles. The reduced vision quality can result in negative effects in practical applications, such as navigation, vision sensing, remote sensing and traffic surveillance, etc. Increasing attention has been paid to single image dehazing [1], i.e., improving image contrast and visibility. Given the current state-of-the-art dehazing progress, the popular methods can be mainly categorized into two types: enhancement-based methods and physics-based methods. Methods of the first type including typical retinex [2] and histogram-based method [3] have been widely utilized. However, these methods do not take into account the image degradation mechanism leading to unstable dehazing performance. Utilization of dark channel prior (DCP) [4] has become one of the most popular and successful physics-based dehazing methods. It is assumed that most local non-sky patches in haze-free images have pixel values close to zero. DCP-based hazing performance has been further improved [5, 6]. DCP-based method easily performs unsatisfactorily in sky regions since the prior is only suitable for non-sky regions. Sky detection and segmentation techniques have been incorporated into traditional dehazing methods [7, 8]. Current research [9] has shown that pixels in a haze-free image can be well approximated using color lines in RGB space. Thus, methods [10, 11] using color lines have improved dehazing performance and gained increasing attention. Haze-relevant features [12] have also contributed to dehazing improvement. More recently, powerful deep learning technique [13, 14] has made great progress in accurate estimation of medium transmission for improving dehazing quality.

Most existing dehazing methods are performed based on the pre-estimation of depth information (or medium transmission). It is generally thought that the dehazing performance highly depends on the accurate depth information (or medium transmission). To guarantee high-quality dehazing, it is necessary to accurately estimate the depth information (or medium transmission) during image dehazing. Fang *et al.* [15] proposed a total variation (TV)-regularized variational framework to simultaneously estimate depth map and haze-free image. TV regularizer is able to preserve the main edges for both depth map and latent sharp image. TV has also been adopted to refine medium transmission to improve the visibility of hazy images [16, 17]. However, TV-based methods often tend to generate staircase-like artifacts in homoge-

This work was supported by the NSFC (No.: 51609195), and the Open Project Program of Key Laboratory of Intelligent Perception and Systems for High-Dimensional Information of Ministry of Education (No.: JYB201704).

neous regions since they favor piecewise constant solutions. As a natural extension of TV regularizer, the total generalized variation (TGV) regularizer of second-order [18, 19] has the capacity of suppressing staircase-like artifacts while preserving fine structures. To further improve dehazing performance, there is a great potential to replace TV by TGV to constrain the estimation of both depth map and haze-free image.

In this work, a TGV-based variational framework is proposed to simultaneously estimate depth map and haze-free image. The main benefit of the proposed framework is that it takes full advantage of the detail-preserving TGV regularizer. Therefore, our dehazing method is capable of preserving the geometric structures for both depth map and haze-free image. In addition, different types of haze situations could also be effectively handled using our method in experiments.

2. PROBLEM FORMULATION

By Koschmieder's law [1], the mathematical formation of a hazy image can naturally be described as follows

$$\mathbf{L}(\mathrm{x}) = \mathbf{J}(\mathrm{x})e^{-k\mathbf{d}(\mathrm{x})} + \mathbf{A}\left(1 - e^{-k\mathbf{d}(\mathrm{x})}\right), \tag{1}$$

where $\mathbf{L}(\mathrm{x})$ is the apparent luminance at pixel $\mathrm{x} \in \Omega$ with Ω being image domain; $\mathbf{J}(\mathrm{x})$ is the haze-free image to be estimated; $\mathbf{A}$ is the atmosphere light, which is assumed to be globally constant; k is the extinction coefficient of the atmosphere and $\mathbf{d}(\mathrm{x})$ denotes the depth of scene. For the sake of convenience, all pixel values of the observed image $\mathbf{L}$ in this work are projected into the interval $[0, 1]$. The original imaging model (1) can be rewritten as follows

$$-\frac{1}{k}\log\left(\mathbf{A} - \mathbf{L}(\mathrm{x})\right) = -\frac{1}{k}\log\left(\mathbf{A} - \mathbf{J}(\mathrm{x})\right) + \mathbf{d}(\mathrm{x}), \tag{2}$$

for $\mathrm{x} \in \Omega$. For the sake of better reading, the index x will be omitted in the rest of this paper. Let $\mathbf{g} = -\frac{1}{k}\log(\mathbf{A} - \mathbf{L})$ and $\mathbf{f} = -\frac{1}{k}\log(\mathbf{A} - \mathbf{J})$, it is easy to obtain that both $\mathbf{g}, \mathbf{f} \in [0, +\infty)$. The estimation of haze-free image $\mathbf{J}$ in Eq. (1) is equivalent to solving the following *pseudo denoising* problem

$$\mathbf{g} = \mathbf{f} + \mathbf{d}, \tag{3}$$

which aims to simultaneously estimate *noise-free image* $\mathbf{f}$ and depth map $\mathbf{d}$ given the observed data $\mathbf{g}$ and pre-estimated atmosphere light $\mathbf{A}$. It is assumed that $\mathbf{f}$ still contain the piecewise affine structures existed in latent sharp image $\mathbf{L}$. To guarantee the dehazing performance, the second-order TGV regularizer on $\mathbf{f}$ is adopted to preserve small-scale structures such as sharp edges. In current literature, TV regularizer has been widely used to estimate the depth map $\mathbf{d}$. However, TV favors piecewise constant solutions, thus the resulting depth map easily suffers from the staircase-like artifacts. It is clear that TV can be regarded as a special case of TGV. To improve the estimation accuracy, the depth map $\mathbf{d}$ is also regularized using TGV constraint because the essential limitations of TV could be significantly suppressed accordingly.

Algorithm 1 Primal-dual algorithm for Step 1

1: **Input**: $\mathbf{g}$, $\mathbf{d}_t$, $\tilde{\alpha_1}$, $\tilde{\alpha_0}$, $\tilde{\delta}$, $\tilde{\tau}$ and $\tilde{\lambda} = 1/\lambda_1$.
2: **while** $j \le J_{\max}$ **do**
3: $\tilde{\mathbf{u}}^{j+1} = \mathrm{proj}_{\tilde{U}}\left(\tilde{\mathbf{u}}^j + \tilde{\delta}\left(\nabla\tilde{\mathbf{f}}^j - \tilde{\mathbf{w}}^j\right)\right)$,
4: $\tilde{\mathbf{v}}^{j+1} = \mathrm{proj}_{\tilde{V}}\left(\tilde{\mathbf{v}}^j + \tilde{\delta}\left(\mathcal{E}\left(\tilde{\mathbf{w}}^j\right)\right)\right)$,
5: $\mathbf{f}_t^{j+1} = \frac{\tilde{\tau}\tilde{\lambda}(\mathbf{g}-\mathbf{d}_t)+\tilde{\mathbf{f}}_t^j+\tilde{\tau}\mathrm{div}\left(\tilde{\mathbf{u}}^{j+1}\right)}{1+\tilde{\tau}\tilde{\lambda}}$,
6: $\mathbf{w}_1^{j+1} = \mathbf{w}_1^j + \tilde{\tau}\left(\tilde{\mathbf{u}}^{j+1} + \mathrm{div}^h\left(\tilde{\mathbf{v}}^{j+1}\right)\right)$,
7: $\tilde{\mathbf{f}}^{j+1} = 2\mathbf{f}_t^{j+1} - \mathbf{f}_t^j$, $\tilde{\mathbf{w}}^{j+1} = 2\mathbf{w}_1^{j+1} - \mathbf{w}_1^j$.
8: **end while**
9: **Output**: $\mathbf{f}_{t+1} \leftarrow \mathbf{f}_t^{J_{\max}}$.

Algorithm 2 Primal-dual algorithm for Step 2

1: **Input**: $\mathbf{g}$, $\mathbf{d}_0$, $\mathbf{f}_{t+1}$, $\bar{\alpha_1}$, $\bar{\alpha_0}$, $\bar{\delta}$, $\bar{\tau}$ and $\bar{\lambda} = (1+\mu)/\lambda_2$.
2: **while** $j \le J_{\max}$ **do**
3: $\bar{\mathbf{u}}^{j+1} = \mathrm{proj}_{\bar{U}}\left(\bar{\mathbf{u}}^j + \bar{\delta}\left(\nabla\bar{\mathbf{d}}^j - \bar{\mathbf{w}}^j\right)\right)$,
4: $\bar{\mathbf{v}}^{j+1} = \mathrm{proj}_{\bar{V}}\left(\bar{\mathbf{v}}^j + \bar{\delta}\left(\mathcal{E}\left(\bar{\mathbf{w}}^j\right)\right)\right)$,
5: $\mathbf{d}_t^{j+1} = \frac{\bar{\tau}\bar{\lambda}((\mathbf{g}-\mathbf{f}_{t+1}+\mu\mathbf{d}_0)/(1+\mu))+\bar{\mathbf{d}}_t^j+\bar{\tau}\mathrm{div}\left(\bar{\mathbf{u}}^{j+1}\right)}{1+\bar{\tau}\bar{\lambda}}$,
6: $\mathbf{w}_2^{j+1} = \mathbf{w}_2^j + \bar{\tau}\left(\bar{\mathbf{u}}^{j+1} + \mathrm{div}^h\left(\bar{\mathbf{v}}^{j+1}\right)\right)$,
7: $\bar{\mathbf{d}}^{j+1} = 2\mathbf{d}_t^{j+1} - \mathbf{d}_t^j$, $\bar{\mathbf{w}}^{j+1} = 2\mathbf{w}_2^{j+1} - \mathbf{w}_2^j$.
8: **end while**
9: **Output**: $\mathbf{d}_{t+1} \leftarrow \mathbf{d}_t^{J_{\max}}$.

2.1. Joint Depth Map Estimation and Image Dehazing

Motivated by the advantage of TGV regularizer, a unified variational model for simultaneously estimating $\mathbf{f}$ and $\mathbf{d}$ from (3) is defined as follows

$$\min_{\mathbf{f},\mathbf{d}}\left\{\frac{1}{2}\left\|\mathbf{g} - (\mathbf{f}+\mathbf{d})\right\|_2^2 + \lambda_1\mathbf{TGV}_{\tilde{\alpha}}^2(\mathbf{f}) + \lambda_2\mathbf{TGV}_{\bar{\alpha}}^2(\mathbf{d}) + \frac{\mu}{2}\left\|\mathbf{d} - \mathbf{d}_0\right\|_2^2\right\}. \tag{4}$$

where λ_1, λ_2 and μ are predefined positive regularization parameters, $\mathbf{d}_0$ is the initial estimation of depth map used to stabilize the final estimation. In this work, $\mathbf{d}_0$ was obtained through the medium transmission map $\mathbf{t}(\mathrm{x}) = e^{-k\mathbf{d}(\mathrm{x})}$, which could be simply estimated using the dark channel prior [4], i.e., $\mathbf{t}(\mathrm{x}) = 1 - \omega\min_c\left(\min_{\mathrm{y}\in\Omega(\mathrm{x})}\left(\frac{\mathbf{L}^c(\mathrm{x})}{\mathbf{A}^c}\right)\right)$ with a predefined parameter $\omega = 0.95$ and a 15×15 region $\Omega(\mathrm{x})$ centered at x. Among the pixels which belong the top 0.1% brightest intensities in the dark channel [4], the pixels with the highest magnitude in $\mathbf{L}$ are selected as the atmospheric light $\mathbf{A}$. The discretized $\mathbf{TGV}_{\tilde{\alpha}}^2(\mathbf{f})$ in (4) is defined as $\mathbf{TGV}_{\tilde{\alpha}}^2(\mathbf{f}) = \min_{\mathbf{e}}\left\{\tilde{\alpha}_1\left\|\nabla\mathbf{f} - \mathbf{e}\right\|_1 + \tilde{\alpha}_0\left\|\mathcal{E}(\mathbf{e})\right\|_1\right\}$ with $\tilde{\alpha}_1$ and $\tilde{\alpha}_0$ being positive parameters. The symmetrized derivative operator $\mathcal{E}$ is given by $\mathcal{E}(\mathbf{e}) = \begin{bmatrix} \partial_x\mathbf{e}_1 & \frac{1}{2}\left(\partial_y\mathbf{e}_1 + \partial_x\mathbf{e}_2\right) \\ \frac{1}{2}\left(\partial_y\mathbf{e}_1 + \partial_x\mathbf{e}_2\right) & \partial_y\mathbf{e}_2 \end{bmatrix}$ with $\mathbf{e} = [\mathbf{e}_1\ \mathbf{e}_2]^T$ being a complex-valued vector field. The

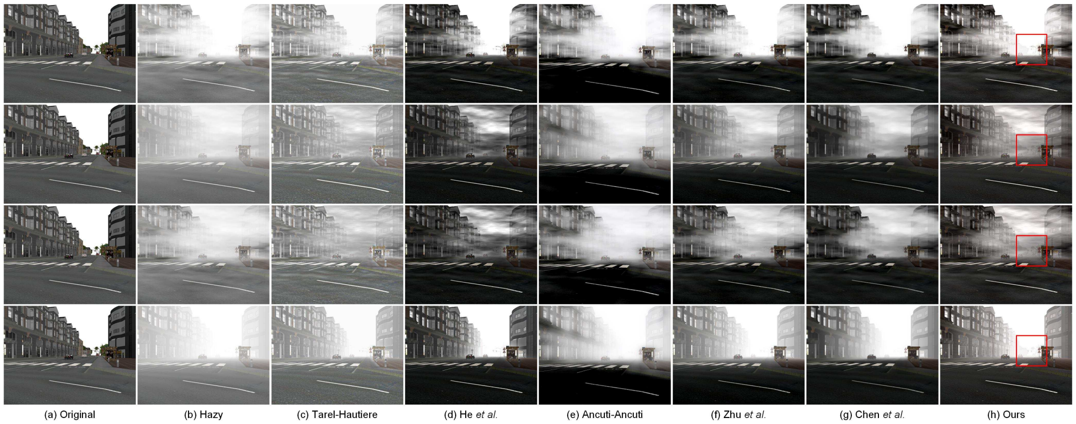

Fig. 1. Comparison of dehazing results on one test image (degraded by 4 different types of haze) from [26]. From left to right: (a) original image, (b) hazy image, restored images generated by (c) Tarel-Hautiere [22], (d) He *et al.* [4], (e) Ancuti-Ancuti [23], (f) Zhu *et al.* [24], (g) Chen *et al.* [25] and (h) ours. (The images are best viewed in full-screen mode.)

definition of $\mathbf{TGV}_{\bar{\alpha}}^2(\mathbf{d})$ can be obtained in the same manner, i.e., $\mathbf{TGV}_{\bar{\alpha}}^2(\mathbf{d}) = \min_{\mathbf{c}} \{\bar{\alpha}_1 \|\nabla \mathbf{d} - \mathbf{c}\|_1 + \bar{\alpha}_0 \|\mathcal{E}(\mathbf{c})\|_1\}$. Due to the nonsmooth nature of TGV regularizer, it is computationally intractable to simultaneously obtain $\mathbf{f}$ and $\mathbf{d}$ via commonly-used numerical methods. It is obvious that the updates of variables $\mathbf{f}$ and $\mathbf{d}$ in (4) are independent of each other. To achieve a stable numerical solution, the nonsmooth convex minimization problem (4) will be effectively solved using a two-step optimization algorithm.

2.2. Numerical Optimization Algorithm

The optimization of original convex minimization problem (4) can be decomposed into the following two steps

$$\text{Step 1}: \mathbf{f}_{t+1} = \min_{\mathbf{f}} \left\{ \frac{\tilde{\lambda}}{2} \|(\mathbf{g} - \mathbf{d}_t) - \mathbf{f}\|_2^2 + \mathbf{TGV}_{\tilde{\alpha}}^2(\mathbf{f}) \right\},$$

$$\text{Step 2}: \mathbf{d}_{t+1} = \min_{\mathbf{d}} \left\{ \frac{\bar{\lambda}}{2} \|(\mathbf{g} - \mathbf{f}_{t+1} + \mu \mathbf{d}_0)/(1+\mu) - \mathbf{d}\|_2^2 + \mathbf{TGV}_{\bar{\alpha}}^2(\mathbf{d}) \right\},$$

for $t = 0, 1, \cdots, T$. Here, $\tilde{\lambda} = 1/\lambda_1$ and $\bar{\lambda} = (1+\mu)/\lambda_2$. Optimizations of Step 1 and 2 will be implemented alternately until the solution converges to the optimal one. In this work, the resulting optimization problems will be solved using the primal-dual algorithm of Chambolle-Pock [20, 21]. Taking the optimization problem of Step 1 as an example. The related dual formulation of this primal problem is given by

$$\min_{\mathbf{f},\tilde{\mathbf{w}}} \max_{\tilde{\mathbf{u}} \in \tilde{U}, \tilde{\mathbf{v}} \in \tilde{V}} \left\{ \frac{\tilde{\lambda}}{2} \|\mathbf{f} - (\mathbf{g} - \mathbf{d}_t)\|_2^2 + \langle \nabla \mathbf{f} - \tilde{\mathbf{w}}, \tilde{\mathbf{u}} \rangle + \langle \mathcal{E}(\tilde{\mathbf{w}}), \tilde{\mathbf{v}} \rangle \right\}$$

with $\tilde{\mathbf{u}}$ and $\tilde{\mathbf{v}}$ being dual variables. The convex variable sets $\tilde{U}$ and $\tilde{V}$ are given by $\tilde{U} = \{\tilde{\mathbf{u}} = (\tilde{u}_1, \tilde{u}_2) \mid \|\tilde{\mathbf{u}}\|_\infty \le \tilde{\alpha}_1\}$ and $\tilde{V} = \left\{ \tilde{\mathbf{v}} = \begin{pmatrix} \tilde{v}_{11} & \tilde{v}_{12} \\ \tilde{v}_{21} & \tilde{v}_{22} \end{pmatrix} \mid \|\tilde{\mathbf{v}}\|_\infty \le \tilde{\alpha}_0 \right\}$. Therefore, the primal-dual algorithm for optimization of Step 1 is detailedly summarized in Algorithm 1. The Euclidean projectors $\mathrm{proj}_{\tilde{U}}(\tilde{\mathbf{u}})$ and $\mathrm{proj}_{\tilde{V}}(\tilde{\mathbf{v}})$ are defined as $\mathrm{proj}_{\tilde{U}}(\tilde{\mathbf{u}}) = \frac{\tilde{\mathbf{u}}}{\max(1, |\tilde{\mathbf{u}}|/\tilde{\alpha}_1)}$ and $\mathrm{proj}_{\tilde{V}}(\tilde{\mathbf{v}}) = \frac{\tilde{\mathbf{v}}}{\max(1, |\tilde{\mathbf{v}}|/\tilde{\alpha}_0)}$, respectively. The definitions of divergence operators $\mathrm{div}(\tilde{\mathbf{u}})$ and $\mathrm{div}^{\hbar}(\tilde{\mathbf{v}})$ are given by $\mathrm{div}(\tilde{\mathbf{u}}) = \partial_x^{-1}\tilde{u}_1 + \partial_y^{-1}\tilde{u}_2$ and $\mathrm{div}^{\hbar}(\tilde{\mathbf{v}}) = \left(\partial_x^{-1}\tilde{v}_{11} + \partial_y^{-1}\tilde{v}_{12}, \partial_x^{-1}\tilde{v}_{21} + \partial_y^{-1}\tilde{v}_{22}\right)^T$. Similarly, Algorithm 2 displays the primal-dual algorithm for the optimization of Step 2. Analogous to the $\mathrm{proj}_{\tilde{U}}(\tilde{\mathbf{u}})$, $\mathrm{proj}_{\tilde{V}}(\tilde{\mathbf{v}})$, $\mathrm{div}(\tilde{\mathbf{u}})$ and $\mathrm{div}^{\hbar}(\tilde{\mathbf{v}})$, the definitions of $\mathrm{proj}_{\bar{U}}(\bar{\mathbf{u}})$, $\mathrm{proj}_{\bar{V}}(\bar{\mathbf{v}})$, $\mathrm{div}(\bar{\mathbf{u}})$ and $\mathrm{div}^{\hbar}(\bar{\mathbf{v}})$ could be easily obtained. The parameters $\tilde{\delta} = \tilde{\tau} = \bar{\delta} = \bar{\tau} = 1/\sqrt{12}$ are predefined to enhance the convergence of primal-dual algorithms. Once the logarithmic-type image $\mathbf{f}$ is obtained, it is easy to yield the haze-free image $\mathbf{J}$ according to Eqs. (2) and (3), i.e.,

$$\mathbf{J} = \mathbf{A} - e^{-k\mathbf{f}}, \tag{5}$$

with $k = 1$ for all results reported in this work.

3. EXPERIMENTS AND DISCUSSION

Comprehensive experiments were implemented on both synthetic and realistic images to compare our method with several popular dehazing methods, i.e., Tarel-Hautiere [22], He *et al.* [4], Ancuti-Ancuti [23], Zhu *et al.* [24] and Chen *et al.* [25]. In all numerical experiments, we manually selected the optimal parameters $\lambda_1 = 1 \times 10^2$, $\lambda_2 = 5 \times 10^1$, $\tilde{\alpha}_1 = \bar{\alpha}_1 = 1 \times 10^{-1}$, $\tilde{\alpha}_0 = \bar{\alpha}_0 = 2 \times 10^{-1}$, $\mu = 5 \times 10^{-1}$ and $J_{\max} = 20$ for our proposed method. Experimental results have demonstrated the effectiveness of these manually-selected parameters under different imaging conditions. For the sake of better comparison, the competing methods generate the most satisfactory dehazing results with the best tuning parameters optimized by the authors.

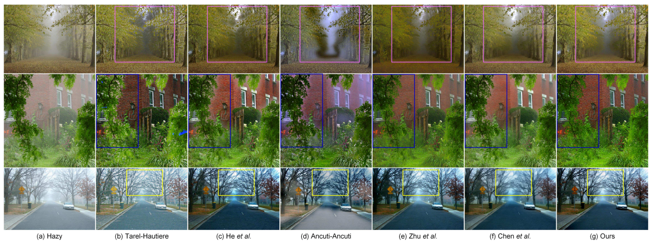

Fig. 2. Comparison of dehazing results on realistic images. From left to right: (a) hazy image, restored images yielded by (b) Tarel-Hautiere [22], (c) He *et al.* [4], (d) Ancuti-Ancuti [23], (e) Zhu *et al.* [24], (f) Chen *et al.* [25] and (g) ours.

Table 1. Comparisons of average PSNR/SSIM results for several different dehazing methods on synthetic dataset [26].

Methods	Haze 1	Haze 2	Haze 3	Haze 4
Tarel-Hautiere [22]	11.54/**0.672**	9.27/0.548	9.37/0.511	11.40/**0.726**
He *et al.* [4]	12.54/0.574	9.69/0.401	9.68/0.372	12.56/0.623
Ancuti-Ancuti [23]	11.16/0.588	11.80/0.482	11.97/0.479	11.00/0.689
Zhu *et al.* [24]	11.17/0.516	11.86/0.459	11.85/0.429	11.09/0.556
Chen *et al.* [25]	11.64/0.551	12.04/0.493	12.01/0.465	11.53/0.586
Ours	**12.81**/0.654	**12.53**/**0.560**	**12.49**/**0.525**	**12.81**/0.704

3.1. Synthetic Experiments

Synthetic experiments were performed on the popular FRIDA2 dataset with a total of 264 hazy images [26]. This dataset contains 66 original images of size 640×480 degraded by 4 different types of haze. Both PSNR and SSIM metrics were selected to assess the competing dehazing methods.Table 1 depicts the quantitative results (i.e., average PSNR and SSIM values) for different dehazing methods under 4 different types of haze. It could be found that our method outperforms other competing methods under consideration in most of the cases. Tarel-Hautiere [22] could sometimes generate the best quantitative results but often leads to the poorest dehazing performance. In contrast, our method is able to robustly perform dehazing under different imaging degradation conditions. The advantage of our method is further confirmed by the visual results shown in Fig. 1. As shown by the red square regions, the proposed method could restore more geometrical structures resulting in improved image quality.

3.2. Realistic Experiments

This subsection evaluates the dehazing performance on several realistic degraded images. Fig. 2 compares our results to state-of-the-art single image dehazing methods [4, 22, 23, 24, 25] on natural images. The methods of Tarel-Hautiere [22], He *et al.* [4], Ancuti-Ancuti [23] and Chen *et al.* [25] easily leave haze in the results, as shown in the color square areas. Zhu *et al.* [24] and our method could effectively remove the haze and enhance the image quality. From the cityscape images in Fig. 3, we can visually find that Zhu *et al.* [24] suffers

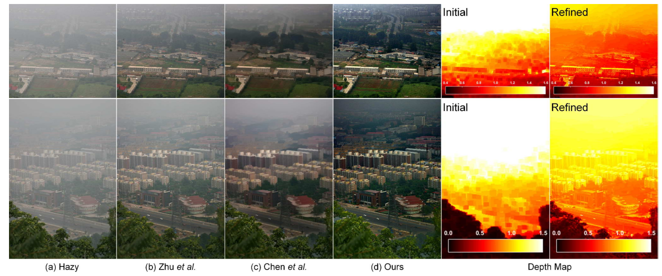

Fig. 3. Comparison of dehazing results on cityscape images.

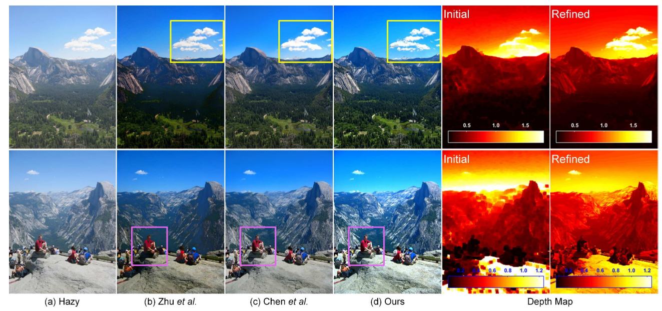

Fig. 4. Comparison of dehazing results on hill images with large sky regions.

from the remaining haze leading to image quality degradation. Chen *et al.* [25] tends to oversmooth the fine-scale image structures. In contrast, our method has the capacity of effectively remove the haze while preserving the image details. Its good performance mainly benefits from the detail-preserving TGV regularizer. Dehazing results in Fig. 4 have also demonstrated the superior performance of our method for hill images with large sky areas. The satisfactory estimations of depth map are visually illustrated in Figs. 3 and 4.

4. CONCLUSIONS

In this paper, we proposed a unified second-order variational framework to simultaneously perform depth map estimation and haze-free image restoration. The introduced second-order regularizer was able to preserve the important structures in depth map and latent image assisting in improving image contrast and visibility. To guarantee stable solutions, a two-step numerical framework was introduced to effectively deal with the nonsmooth optimization problems related to depth map estimation and latent image restoration. Experiments on both synthetic and realistic images have been implemented to illustrate the satisfactory performance of our method in terms of quantitative assessment and visual quality. It should be pointed out that the proposed method performs image dehazing on each channel and combines the restored channels into a color image. To further enhance dehazing performance, the multichannel version of TGV [27] can be extended to constrain the latent sharp image $\mathbf{f}$ in Eq. (4) in our future work.

5. REFERENCES

[1] R. Fattal, "Single image dehazing," *ACM Trans. Graph.*, vol. 27, no. 3, pp. 72, Aug. 2008.

[2] S. Zhang, T. Wang, J. Dong, and H. Yu, "Underwater image enhancement via extended multi-scale Retinex," *Neurocomputing*, vol. 245, pp. 1-9, Jul. 2017.

[3] J. H. Kim, W. D. Jang, J. Y. Sim, and C. S. Kim, "Optimized contrast enhancement for real-time image and video dehazing," *J. Vis. Commun. Image Represent.*, vol. 24, no. 3, pp. 410-425, Apr. 2013.

[4] K. He, J. Sun, and X. Tang, "Single image haze removal using dark channel prior," *IEEE TPAMI*, vol. 33, no. 12, pp. 2341-2353, Dec. 2011.

[5] Y. Xu, J. Wen, L. Fei, and Z. Zhang, "Review of video and image defogging algorithms and related studies on image restoration and enhancement," *IEEE Access*, vol. 4, pp. 165-188, 2016.

[6] Y. Li, S. You, M. S. Brown, and R. T. Tan, "Haze visibility enhancement: A survey and quantitative benchmarking," *Comput. Vis. Image Underst.*, vol. 165, pp. 1-16, 2017.

[7] Y. Liu, H. Li, and M. Wang, "Single image dehazing via large sky region segmentation and multiscale opening dark channel model," *IEEE Access*, vol. 5, pp. 8890-8903, 2017.

[8] W. Wang, X. Yuan, X. Wu, and Y. Liu, "Dehazing for images with large sky region," *Neurocomputing*, vol. 238, pp. 365-376, May 2017.

[9] I. Omer and M. Werman, "Color lines: Image specific color representation," In *Proc. IEEE CVPR*, Washington, DC, USA, Jul. 2004, pp. 946-953.

[10] R. Fattal, "Dehazing using color-lines," *ACM Trans. Graph.*, vol. 34, no. 1, pp. 13, Nov. 2014.

[11] D. Berman and S. Avidan, "Non-local image dehazing," In *Proc. IEEE CVPR*, Las Vegas, NV, USA, Jun. 2016, pp. 1674-1682.

[12] K. Tang, J. Yang, and J. Wang, "Investigating haze-relevant features in a learning framework for image dehazing," In *Proc. IEEE CVPR*, Columbus, OH, USA, Jun. 2014, pp. 2995-3000.

[13] W. Ren, S. Liu, H. Zhang, J. Pan, X. Cao, and M. H. Yang, "Single image dehazing via multi-scale convolutional neural networks," In *Proc. ECCV*, Amsterdam, The Netherlands, Oct. 2016, pp. 154-169.

[14] B. Cai, X. Xu, K. Jia, C. Qing, and D. Tao, "Dehazenet: An end-to-end system for single image haze removal," *IEEE TIP*, vol. 25, no. 11, pp. 5187-5198, Nov. 2016.

[15] F. Fang, F. Li, and T. Zeng, "Single image dehazing and denoising: A fast variational approach," *SIAM J. Imaging Sci.*, vol. 7, no. 2, pp. 969-996, 2014.

[16] L. Li, W. Feng, and J. Zhang, "Contrast enhancement based single image dehazing via TV-l1 minimization," In *Proc. IEEE ICME*, Chengdu, China, Jul. 2014, pp. 1-6.

[17] X. Liu, F. Zeng, Z. Huang, and Y. Ji, "Single color image dehazing based on digital total variation filter with color transfer," In *Proc. IEEE ICIP*, Melbourne, VIC, Australia, Sep. 2013, pp. 909-913.

[18] K. Bredies, K. Kunisch, and T, Pock, "Total generalized variation," *SIAM J. Imaging Sci.*, vol. 3, no. 3, pp. 492-526, 2010.

[19] R. W. Liu, L. Shi, C. H. Simon, and D. Wang, "Box-constrained second-order total generalized variation minimization with a combined L1,2 data-fidelity term for image reconstruction," *J. Electron. Imaging*, vol. 24, no. 3, pp. 033026, Jun. 2015.

[20] A. Chambolle and T. Pock, "A first-order primal-dual algorithm for convex problems with applications to imaging," *J. Math. Imaging Vis.*, vol. 40, no. 1, pp. 120-145, May 2011.

[21] L. Condat, "A primal-dual splitting method for convex optimization involving Lipschitzian, proximable and linear composite terms," *J. Optim. Theory Appl.*, vol. 158, no. 2, pp. 460-479, Aug. 2013.

[22] J. P. Tarel and N. Hautiere, "Fast visibility restoration from a single color or gray level image," In *Proc. IEEE ICCV*, Kyoto, Japan, Sep. 2009, pp. 2201-2208.

[23] C. O. Ancuti and C. Ancuti, "Single image dehazing by multi-scale fusion," *IEEE TIP*, vol. 22, no. 8, pp. 3271-3282, May 2013.

[24] Q. Zhu, J. Mai, and L. Shao, "A fast single image haze removal algorithm using color attenuation prior," *IEEE TIP*, vol. 24, no. 11, pp. 3522-3533, Nov. 2015.

[25] C. Chen, M. N. Do, and J. Wang, "Robust image and video dehazing with visual artifact suppression via gradient residual minimization," In *Proc. ECCV*, Amsterdam, The Netherlands, Oct. 2016, pp. 576-591.

[26] J. P. Tarel, N. Hautière, L. Caraffa, A. Cord, H. Halmaoui, and D. Gruyer, "Vision enhancement in homogeneous and heterogeneous fog," *IEEE ITSM*, vol. 4, no. 2, pp. 6-20, Apr. 2012.

[27] F. Knoll, M. Holler, T. Koesters, R. Otazo, K. Bredies, and D. K. Sodickson, "Joint MR-PET reconstruction using a multi-channel image regularizer," *IEEE TMI*, vol. 36, no. 1, pp. 1-16, Jan. 2017.